

# Time Series Classification via Topological Data Analysis

Alperen Karan and Atabey Kaygun

November 1, 2021

## Abstract

In this paper, we develop topological data analysis methods for classification tasks on univariate time series. As an application we perform binary and ternary classification tasks on two public datasets that consist of physiological signals collected under stress and non-stress conditions. We accomplish our goal by using persistent homology to engineer stable topological features after we use a time delay embedding of the signals and perform a subwindowing instead of using windows of fixed length. The combination of methods we use can be applied to any univariate time series and in this application allows us to reduce noise and use long window sizes without incurring an extra computational cost. We then use machine learning models on the features we algorithmically engineered to obtain higher accuracies with fewer features.

## 1 Introduction

In this study, we use persistent homology to perform classification tasks on two publicly available multivariate time series datasets [19, 11] that include physiological data collected during stressful and non stressful tasks. Instead of directly computing signal-specific features from *sliding windows* and *subwindows* on modalities such as electrocardiogram and wrist temperature (Figure 7), we extracted features using *persistence diagrams* and their statistical properties. Subwindowing method allowed us to reduce noise without incurring an extra computational cost. We then developed machine learning models and assess the performance of our models by varying window sizes and using different flavors of persistence diagrams.

Topological Data Analysis (TDA) techniques usually work with points embedded in an affine space of large enough dimension. However, TDA techniques can still be applied to time series data sets whether they are univariate or multivariate. One can convert a univariate time series into a finite collection of points in a  $d$ -dimensional affine space using *delay embedding* methods, of which one can compute persistent homology. Since Taken's Theorem implies that the delay embeddings produces topologically invariant subsets on a non-chaotical dynamical system [21], one can reasonably expect that persistent homology produces features that would distinguish different time series.

There is a handful of research on the persistent homology of delay embeddings for time series classification [23, 20, 1]. There are also density based [8] and subsampling methods [10]

used in calculations of persistent homology of delay embeddings, but these studies use sliding windows of a fixed length. Such methods create training datasets of a fixed dimension from data sets containing non-necessarily equally sized time series. However, if the chosen window size is long, the delay embedding might produce large datasets for which computational cost of persistent homology is prohibitive.

In this study, we explicitly rely on features we algorithmically engineer using persistent homology, specifically persistence diagrams and their metric and statistical properties. The *Bottleneck* and *Wasserstein* metrics are the two metrics we are going to use to calculate distances between persistence diagrams. Since these metrics are computationally expensive, the use of distance-based machine learning models on persistence diagrams (such as kNN) are preferred only when the training subset is fairly small [13]. When the dataset is large, one must resort to using secondary methods to extract features from persistence diagrams first. In such cases, one must rely on engineered feature vectors and machine learning models developed on these feature vectors. We refer the reader to [18] for a survey of different techniques.

In our study, we start with using sliding windows of a fixed size since this is going to allow us to compare our findings with the original studies [19, 11]. Moreover, within each window we run another sliding window (which we will call a *subwindow*) with a much shorter length, yet long enough to contain at least one cycle of periodic-like signals. Thus the subwindows capture the local information about window they were taken, and one can measure statistically how these local features vary over the window. We specifically created different delay embeddings with different embedding sizes, and then constructed topologically stable features from the resulting persistence diagrams. Finally, we trained and tested machine learning models on these newly engineered features.

## 1.1 Plan of the article

The rest of this paper is set up as follows. In Section 2, we start by reviewing persistent homology, metrics and kernels on the space of persistence diagrams. The section ends with feature engineering on persistence diagrams using the metrics and kernels defined. In Section 3, we investigate sliding windows and time delay embeddings of univariate time series, and we demonstrate how feature engineering on sliding subwindows is independent from any window size. In Section 4, we discuss the datasets, and we explain our methodology in detail in Section 5. We then present our results and their analysis in Section 6 and Section 7.

## 2 Topological Data Analysis and Persistent Homology

Assume we work within the metric space  $\mathbb{R}^n$  with a fixed distance function  $d$  for a fixed  $n \geq 1$ . The reader might assume  $d$  is the euclidean metric even though the arguments we provide work equally well with any other metric. Assume we have a finite sample of points  $X$  from an unknown region  $\Omega$  in  $\mathbb{R}^n$ . Our ultimate aim is to gain some insight into topological/homological invariants of  $\Omega$  calculating homologies of a sequence of complexes we write out of  $X$ .

## 2.1 Simplices

Given a finite set of points  $X$  in  $\mathbb{R}^n$ , the simplex  $S(X)$  spanned by  $X$  is the convex subset of  $\mathbb{R}^n$  spanned by  $X$ . In other words  $S(X)$  is

$$S(X) = \left\{ \sum_{\mathbf{x} \in X} \lambda_{\mathbf{x}} \mathbf{x} \mid \lambda_{\mathbf{x}} \in [0, 1] \text{ for every } \mathbf{x} \in X \text{ and } 1 = \sum_{\mathbf{x}} \lambda_{\mathbf{x}} \right\}$$

The points in  $X$  are called *the vertices* of the simplex  $S(X)$ . We usually order these points with a chosen well-order and write  $[\mathbf{x}_1, \dots, \mathbf{x}_m]$  for the simplex spanned by this set. This amounts to choosing a specific orientation for each of the faces of the simplex.

Any subset  $Y \subseteq X$  spans a subcomplex  $S(Y)$  defined again as the convex combination of points in  $Y$ . These are called *faces* of the complex  $S(X)$ . The dimension of the face, and therefore the simplicial complex itself, is determined by the number of points. For example, 0-dimensional faces are the vertices, 1-dimensional faces are line segments connecting vertices etc. (see Figure 1).

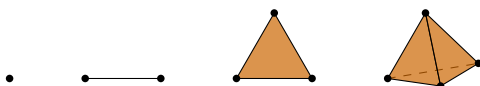


Figure 1: Simplices of dimension 0 through 3.

## 2.2 Simplicial complexes

An  $m$ -dimensional *simplicial complex*  $C_* = (C_0, \dots, C_m)$  in  $\mathbb{R}^n$  is a finite collection of simplices such that each subset  $C_i$  contains the set of its simplices of dimension  $i$ . A complex satisfies the condition that given any two simplices  $S$  and  $S'$  in  $C_*$  the intersection  $S \cap S'$  is a face subsimplex of both  $S$  and  $S'$  (see Figure 2.) The dimension of a simplicial complex  $C_*$  is defined as the maximal dimension among all of the simplicial contained in  $C_*$ .

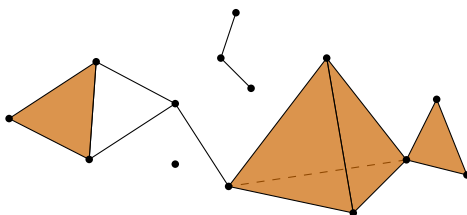


Figure 2: A simplicial complex.

## 2.3 Homology of a complex

Assume we are already given a simplicial complex  $C_* = C_1, \dots, C_m$  in  $\mathbb{R}^n$  where we keep track of each of the simplices with a fixed dimension- $i$  as  $C_i$ . In other words,  $C_0$  is the collection of vertices of our complex,  $C_1$  is the set of all line segments between these vertices,  $C_2$  is the set of all 2-simplices in  $C_*$  etc. Now, for each  $i > 0$  we form a  $\mathbb{R}$ -vector space  $\text{Span}(C_i)$  spanned by

$i$ -dimensional simplices of  $C_*$  together with operators  $d_i: \text{Span}(C_i) \rightarrow \text{Span}(C_{i-1})$  defined as follows: given an  $i$ -simplex  $[\mathbf{x}_1, \dots, \mathbf{x}_i]$  the operator  $d_i$  is given as

$$d_i[\mathbf{x}_1, \dots, \mathbf{x}_i] = \sum_{j=1}^i (-1)^j [\mathbf{x}_1, \dots, \widehat{\mathbf{x}}_j, \dots, \mathbf{x}_i] \quad (1)$$

where  $\widehat{\mathbf{x}}_j$  indicates that specific vertex is missing. Now, we have  $d_{i-1}d_i = 0$  for every  $i > 1$  which means  $\ker(d_i) \supseteq \text{im}(d_{i+1})$ . Since every basis of  $\text{im}(d_{i+1})$  can be completed to a basis of  $\ker(d_i)$ , one can define  $H_i(C_*)$  as the subspace of  $C_i$  spanned by vectors in  $\ker(d_i)$  which are not in  $\text{im}(d_{i+1})$  for every  $i \geq 0$ . For each  $i \geq 0$ , the number  $\dim_{\mathbb{R}} H_i(C_*)$  is called the  $i$ -th Betti number of the complex  $C_*$ .

## 2.4 Rips complexes

One of the most commonly used simplicial complexes obtained out of a finite sample of points is the *Rips complex*. Given  $X$  and  $\varepsilon > 0$ , we say that a finite set of points  $U \subset X$  in  $X$  forms a simplex in  $\text{Rips}(X, \varepsilon)$  if every pair of points in  $\mathbf{x}, \mathbf{y} \in U$  are at-most  $\varepsilon$ -apart. In other words

$$S(U) \in \text{Rips}(X, \varepsilon) \text{ if and only if } d(\mathbf{x}, \mathbf{y}) \leq \varepsilon \text{ for every } \mathbf{x}, \mathbf{y} \in U$$

Hence an edge occurs between two vertices when their  $\varepsilon/2$  balls intersect; and a 2-simplex occurs whenever all edges of the 2-simplex are already present. Observe that for  $\varepsilon = 0$  the Rips complex consists only of the sampled vertices  $X$  which is our the data set. Moreover, for very large  $\varepsilon$  the Rips complex becomes a single high dimensional simplex since we have a finite sample of points.

## 2.5 Filtrations

A growing sequence of simplicial complexes is called a *filtration*. In other words a filtration is a collection of complexes  $F_\varepsilon$  such that  $F_{\varepsilon_1} \subseteq F_{\varepsilon_2}$  whenever  $\varepsilon_1 \leq \varepsilon_2$ . The sublevel sets  $f^{-1}(-\infty, \varepsilon]$  induce a filtration from a continuous function  $f: S \rightarrow \mathbb{R}$  where  $S \subseteq \mathbb{R}$ , because the sublevel sets is a growing set of intervals. When  $S \subseteq \mathbb{R}^d$  with  $d > 1$ , the sublevel sets are not generally simplicial complexes. However, we can approximate them with Rips complexes, and get a Rips filtration:  $\varepsilon_1 \leq \varepsilon_2$  implies  $\text{Rips}(X, \varepsilon_1) \subseteq \text{Rips}(X, \varepsilon_2)$  (Figure 3).

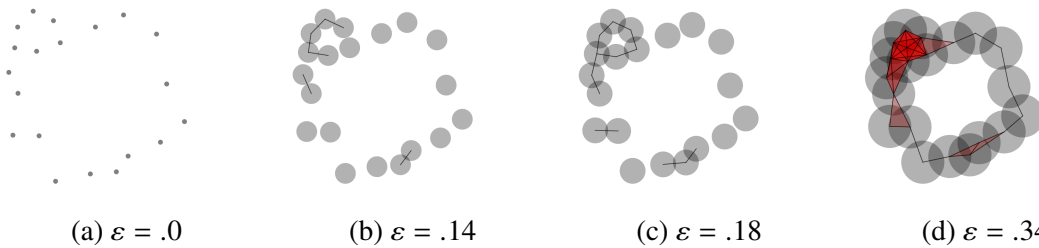


Figure 3: The Rips complex  $\text{Rips}(X, 2\varepsilon)$  (black and red) of a sample dataset  $X$  (grey) drawn at different scales. At  $\varepsilon = .18$ , there are 10 components and one hole. At  $\varepsilon = .34$  there is one component and one hole.

We can compute the homology of a Rips complex at a particular  $\varepsilon_0$ , however, a choice of  $\varepsilon_0$  at which the Rips complex has the homology type of  $\Omega$  may not necessarily exist unless  $X \subseteq \Omega$  is  $\varepsilon$ -dense for some  $\varepsilon^1$ . So, we need to look at the “persistent” features of the homology of the data at different scales of  $\varepsilon$  in order to see which homology classes live for a small range of  $\varepsilon$ , and which homology classes persist longer.

## 2.6 Persistent homology

Consider a filtration  $(K_\varepsilon)_{\varepsilon \in I}$  of simplicial complexes. Although in theory  $I$  can be infinite, in practice we can assume  $|I| = m < \infty$  since computers have a limited memory. By definition of a filtration,  $\varepsilon_i \leq \varepsilon_j$  implies  $K_{\varepsilon_i} \subseteq K_{\varepsilon_j}$ . This relation yields a linear map between the homology groups  $H_n(K_{\varepsilon_i}) \rightarrow H_n(K_{\varepsilon_j})$  for arbitrary  $n$ . This yields a *persistence module*

$$H_n(K_{\varepsilon_1}) \rightarrow H_n(K_{\varepsilon_2}) \rightarrow \cdots \rightarrow H_n(K_{\varepsilon_m})$$

and whenever  $I$  is finite [5]. Moreover, there is an interval  $[b, d]$  where  $b$  is the minimum filtration index where a  $H_n(K_{\varepsilon_b})$  is non-zero, and  $d$  is the minimum filtration index after which  $H_n(K_{\varepsilon_\ell})$  is all 0. The numbers  $b$  and  $d$  are called *the birth* and *the death* of the corresponding homological features.

A multiset, where a point  $(b_i, d_i)$  may appear more than once, called the *persistence diagram* [9], with *birth* and *death* axes is usually used to visualize persistent homology. A nice property of persistent homology is that any two decompositions of the same persistence module is just a permutation of the interval modules in the direct sum, not affecting the resulting persistence diagram. A persistence diagram is assumed to contain infinitely many copies of the *diagonal* which includes the points with simultaneous birth and death. This allows us to create bijections between two persistence diagrams.

## 2.7 Wasserstein and Bottleneck distances

Let  $D_1, D_2$  be persistence diagrams (along with their diagonals) and  $\gamma : D_1 \rightarrow D_2$  be a bijection. The *bottleneck distance*  $W_\infty$  [6] between  $D_1$  and  $D_2$  is defined as follows (see Figure 4):

$$W_\infty(D_1, D_2) := \inf_\gamma \sup_{x \in D_1} \|x - \gamma(x)\|_\infty.$$

The *p-Wasserstein distance* [7] is defined similarly:

$$W_p(D_1, D_2) := \inf_\gamma \left( \sum_{x \in D_1} \|x - \gamma(x)\|_\infty^p \right)^{\frac{1}{p}}.$$

The Bottleneck distance is stable under small perturbations of the data, and the *p-Wasserstein distance* is stable under certain assumptions.

---

<sup>1</sup>A subset  $X \subseteq \Omega$  is called  $\varepsilon$ -dense if for every  $\mathbf{x} \in \Omega$  there is a point  $\mathbf{y} \in X$  such that  $d(\mathbf{x}, \mathbf{y}) < \varepsilon$ . See [3] and [15, page 10].

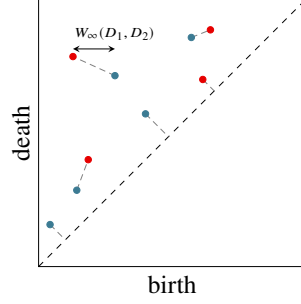


Figure 4: The bottleneck distance between two persistence diagrams.

## 2.8 Persistence landscapes and Betti curves

Let  $D$  be a persistence diagram and  $\alpha = (b_\alpha, d_\alpha)$  be a point in the diagram. First consider the following function  $f_\alpha$  which is 1 between birth and death, and zero everywhere else:

$$f_\alpha(x) := \begin{cases} 1, & b_\alpha \leq x \leq d_\alpha \\ 0, & \text{otherwise} \end{cases}.$$

Then the *Betti Curve* (Figure 5b) obtained from  $D$  is the sum

$$Betti_D(x) := \sum_{\alpha \in D} f_\alpha(x).$$

Persistence landscapes, introduced by Bubenik [4], is another statistical summary function that can be obtained from a persistence diagram  $D$  (Figure 5c). Given  $\alpha \in D$ , let

$$g_\alpha(x) := \begin{cases} x - b_\alpha, & \text{if } b_\alpha \leq x \leq (b_\alpha + d_\alpha)/2 \\ d_\alpha - x, & \text{if } (b_\alpha + d_\alpha)/2 < x \leq d_\alpha \\ 0, & \text{otherwise} \end{cases}$$

Then, the  $k^{\text{th}}$  layer persistence landscape of  $D$  is defined as

$$Landscape_D^k(x) := \text{kmax}_{\alpha \in D} g_\alpha(x)$$

where  $\text{kmax}$  is the  $k^{\text{th}}$  maximum value among a finite set. In this study, we use the first layer persistence landscapes, and we will drop the superscript  $k = 1$ .

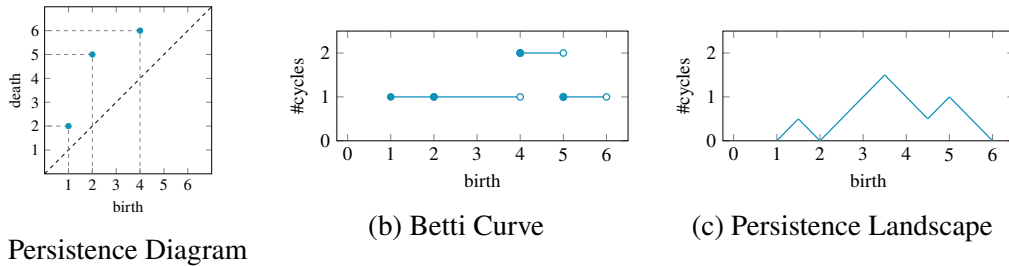


Figure 5: A persistence diagram (a), its Betti Curve (b) and Persistence Landscape (c).

## 2.9 Feature engineering on persistence diagrams

There are several ways to construct features from a persistence diagram, such as calculating the mean birth times of points in the diagram. However, these features are not stable in the sense that a slight perturbation in the dataset can create or remove several points with short lifetimes.

### 2.9.1 Via Bottleneck and Wasserstein distances

Let  $D_\emptyset$  be the diagram containing only the diagonal. For any diagram  $D$ , we can compute the Wasserstein distance for  $p = 1$ :  $W_1(D, D_\emptyset)$  and the bottleneck distance  $W_\infty(D, D_\emptyset)$  as two features of a diagram. Let  $l_x$  be the lifetime of a point  $x \in D$ . We can write them down explicitly since the perfect matching between any diagram  $D$  with  $D_\emptyset$  is obvious:

$$W_1(D, D_\emptyset) = \frac{1}{\sqrt{2}} \sum_{x \in D} (l_x) \quad W_\infty(D, D_\emptyset) = \frac{1}{\sqrt{2}} \sup_{x \in D} (l_x)$$

### 2.9.2 Via persistent entropy

Persistent Entropy is another summary statistic that can be derived from a persistence diagram [2]. A key feature of persistent entropy is that it is scale invariant. The persistent entropy  $PE(D)$  of persistence diagram  $D$  is given by

$$PE(D) := \sum_{x \in D} -\frac{l_x}{L_D} \ln \left( \frac{l_x}{L_D} \right)$$

where  $L_D := \sum_{x \in D} l_x$  is the sum of lifetimes. Whenever the diagram contained only the diagonal, the persistent entropy was assumed to be zero.

### 2.9.3 Via norms

Finally, we consider the Betti curve and first layer persistence landscape of a diagram  $D$  as real valued functions, and then compute their  $L^1$  and  $L^2$  norms. These are going to constitute our four new features constructed from these kernels.

## 3 Sliding Windows and Delay Embeddings

### 3.1 Converting univariate series into multivariate series

Let  $x = (x_i : i = 0, \dots, N)$  be a univariate time series in  $\mathbb{R}$ . The sequence of *sliding windows* on  $x$  with a window shift of  $k$  is a sequence of equally sized multivariate time series:

$$((x_{kn}, x_{kn+1}, x_{kn+2}, \dots, x_{kn+d-1}) : n = 0, 1, \dots, \lfloor (N - d + 1)/k \rfloor).$$

Creating equally sized shorter windows from a large time series can be very useful for machine learning tasks. Note, however, that when the window shift is smaller than the window size, the

sliding windows are overlapping. In such cases, to prevent data leakage between train and test sets, train-test splits should be carefully made.

## 3.2 Delay embeddings

The method of *delay embeddings*, which is similar to sliding windows method, regards each sliding window as a data point in  $d$  dimensional space. That is, the  $d$  dimensional delay embedding (also known as a *state space reconstruction*) of  $x$  with a shift of  $k$  is the subset of  $\mathbb{R}^d$  given by

$$\{(x_{kn}, x_{kn+1}, x_{kn+2}, \dots, x_{kn+d-1}) : n = 0, 1, \dots, \lfloor (N - d + 1)/k \rfloor\}.$$

The number  $d$  is referred as the dimension or the size of the delay embedding.

One should note that if  $y$  is a periodic signal, the time delay embedding on  $y$  will follow a closed path on  $\mathbb{R}^d$ . For example, the time delay embeddings of  $y = \{\cos x : x \in \mathbb{T}\}$ , where  $\mathbb{T}$  is a set of equally spaced points on  $\mathbb{R}$ , lies on a circle if the embedding dimension resonate with the frequency of  $\cos x$  [17].

### 3.2.1 An example

The two time series of length 250 in Figure 6 are sampled from five periods of  $y = \sin x$  and  $y = \sin^5 x$  with additional noise, respectively. The time delay embeddings with  $d = 50$  for both time series are both circles with different radii. However, when the embedding dimension is small ( $d = 15$ ), the the former is an ellipse whereas the latter is the boundary of an eyeglasses shaped object. This idea shows us that for different embedding dimensions, we can distinguish the two time series using persistent homology.

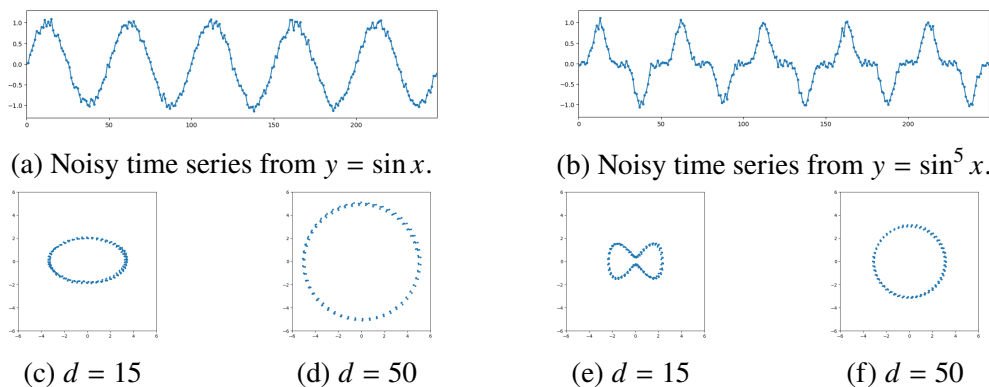


Figure 6: Two noisy time series data along with their time delay embeddings for  $d = 15$  and  $d = 50$  under PCA visualization.

## 3.3 The subwindowing method

Assume that we would like to compute features on a set of sliding windows with a fixed window size and fixed window shift. Instead of directly computing features on each window,



we can create sliding *subwindows* on each window (Figure 7), then compute the features at the subwindows. Looking at the average and the standard deviation of the subwindow features, one can understand how the window behaves locally, and how this local behavior varies over time.

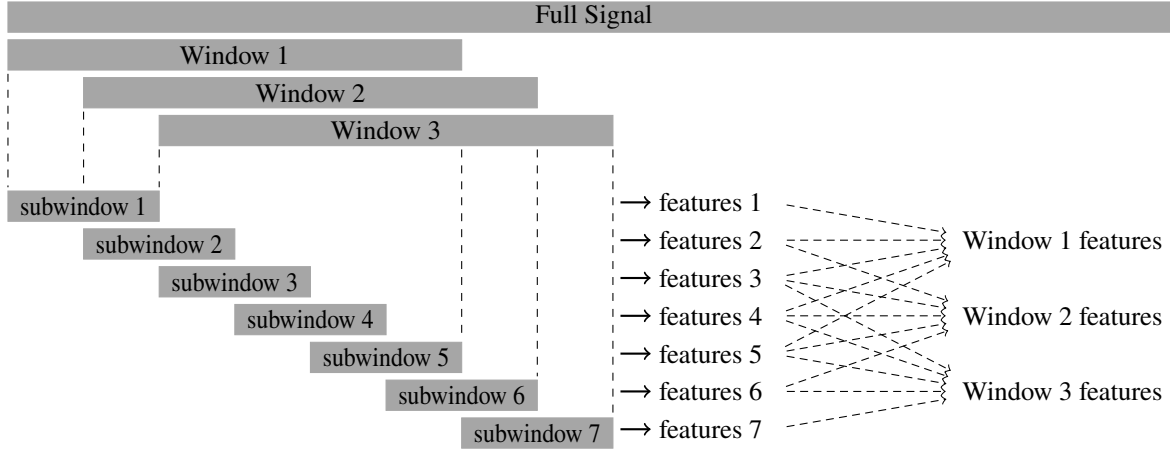


Figure 7: The subwindowing method for feature construction

This approach is especially useful if we want to compute topological features on windows using persistent homology on delay embeddings. If a window contains a noisy part (as most physiological signals do), the corresponding delay embedding and the resulting persistence diagrams will be noisy as well. With subwindowing, the noise is trapped into a few subwindows, and its effects on the feature vector of a window diminish largely by computing mean and standard deviation of feature vectors of subwindows.

Moreover, the subwindowing have advantages for computation. Assume that the window features are obtained by finding the mean and standard deviation of the features from subwindows. Assume also that the subwindow shift is the same as window shift as in Figure 7. Now, let Window  $N$  and Window  $N + 1$  be two consecutive windows with subwindows  $sw_1, \dots, sw_M$  and  $sw_2, \dots, sw_{M+1}$ , respectively. Let  $f_i$  be the feature coming from  $sw_i$ . Then, the mean feature for Window  $N$  is

$$\mu_N := \frac{1}{M} \sum_{i=1}^M f_i$$

and the standard deviation of features for Window  $N$  is

$$\sigma_N := \sqrt{\frac{1}{M} \sum_{i=1}^M (f_i - \mu_N)^2}.$$

Observe that

$$\mu_{N+1} = \frac{1}{M} \sum_{i=2}^{M+1} f_i = \left( \frac{1}{M} \sum_{i=1}^M f_i \right) + \frac{f_{M+1} - f_1}{M} = \mu_N + \frac{f_{M+1} - f_1}{M}.$$

Also,

$$\begin{aligned} M(\sigma_{N+1}^2 - \sigma_N^2) &= \left( \sum_{i=2}^{M+1} (f_i - \mu_{N+1})^2 \right) - \left( \sum_{i=1}^M (f_i - \mu_N)^2 \right) \\ &= (f_{M+1}^2 - f_1^2) - 2(2\mu_{N+1} - f_{M+1}^2 - 2\mu_N + f_1^2) + M(\mu_{N+1}^2 - \mu_N^2) \end{aligned}$$

So,  $\mu_{N+1}$  can be written in terms of  $\mu_N, f_1, f_{M+1}$  and  $M$ . Similarly,  $\sigma_{N+1}$  can be written as a function of  $\sigma_N, \mu_N, f_1, f_{M+1}$  and  $M$ .

This means once the mean and standard deviation for a window is computed, these features for the next sliding windows can be computed continuously regardless of the window size. If the sampling frequency of the signal is high, and if the window size is large, then computing features directly from the windows can be difficult. Subwindowing allows us to compute the features in the same time regardless of the window size.

## 4 Dataset Description

We used two publicly available datasets to show how persistent homology can be used for affect and stress recognition: the WESAD dataset [19] and the DriveDB dataset [11]. In each dataset, participants were subjected to some stress and non-stress conditions in different environments. Physiological signals were collected during the experiments with different devices. The datasets are shortly described below.

### 4.1 The WESAD dataset

Physiological recordings from a wrist (Empatica E4) and a chest (RespiBAN) worn device were collected from 15 participants during three different conditions: baseline, stress and amusement (Figure 8a). All participants started the experiment with the baseline condition in which they did normal activities such as reading a magazine or sitting at a table approximately for 20 minutes. In the stress condition, participants went under the Trier Social Stress Test (TSST) which included doing a 5-minute presentation to an audience and counting backwards from 2023 with steps of 17. The stress condition lasted about 10 minutes. The amusement condition consisted of watching a sequence of funny video clips which lasted about 7 minutes. Each of the three conditions were followed by a meditation phase aiming to bring subjects to a neutral state. The order of stress and amusement conditions were counterbalanced across participants.

Acceleration (ACC), respiration (RESP), electrocardiogram (ECG), electrodermal activity (EDA), electromyography (EMG) and temperature (TEMP) signals were collected from the chest worn device at 700 Hz. The signals from the wrist worn device were ACC, blood volume pulse (BVP), EDA and TEMP, with sampling frequencies 32 Hz, 64 Hz, 4 Hz and 4 Hz, respectively.

### 4.2 The DriveDB dataset

In this study, a total of 17 participants were recorded under three stress levels. The low and high stress conditions correspond to driving on the highway and in the city (Figure 8b). The

experiment started with resting in the car, then driving on the highway and in the city several times and finally ending the experiment with the rest condition again. The experiment lasted about 60-90 minutes, depending on participants' driving speeds. The physiological signals that were recorded during the experiments ECG, EMG, galvanic skin response (GSR) from foot and hand, heart rate (HR) and RESP. The sampling frequency for all signals were 15.5 Hz. Recordings of only 9 participants were analyzed since the markers that shows the transition between different stress conditions were not available or legible for others.

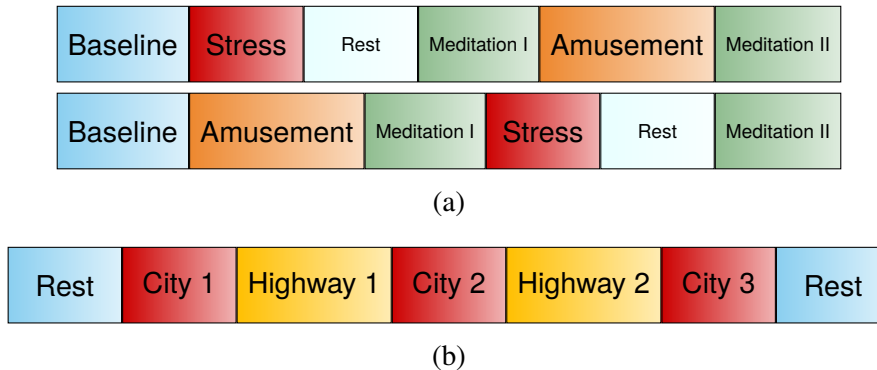


Figure 8: The study protocols for WESAD (a) and DriveDB (b) datasets.

## 5 Methodology

All signals from both datasets were split by stress condition and by participant. To reduce computational time, all signals with a sampling rate higher than 100 Hz (*i.e.* chest signals from WESAD) were downsampled to 100 Hz. Moreover, signals from DriveDB dataset were upsampled from 15.5 Hz to 16 Hz to ensure consistency in our method. Resampling from 700 Hz to 100 Hz was done by selecting every 7th element in the discrete time series, and resampling from 15.5 Hz to 16 Hz was done by upsampling to 496 Hz using linear interpolation, then downsampling by selecting every 31th element. The ACC data in WESAD contained three time series, for the accelerations in  $x$ ,  $y$ , and  $z$  axes; we averaged them to get a single time series.

### 5.1 Sliding windows and subwindows

Our goal is to create topological features from the windows and use it for affect and stress recognition. Sliding windows with duration 60 seconds and a shift of 2 seconds were created for both WESAD and DriveDB datasets. Then, subwindows with 4s duration and 2s shift were created. The subwindowing method was useful in our study for several reasons. First, stressful events usually induce irregular physiological responses. For example, a typical response to stress is high heart rate variability. So, looking at how the subwindows behave across a window is informative for the current task. That is, subwindowing helps us understand the local topology of the window. Secondly, even in non-stress conditions, brief yet powerful noises are common due to participants' coughing, sudden movements etc. (e.g. Figure 9). Third, the delay embedding of a window is a very large dataset (especially if the sampling frequency is high such as 100 Hz), making the computation of persistent homology impractical.

Our empirical tests showed that the subwindow size of 4 seconds is long enough to capture the local information about the physiological signal, yet it is also short enough to make computation of persistent homology (induced by the delay embeddings) very fast. We will then look at the mean and variance of the features extracted from the subwindows within each window, and feed them into the machine learning algorithm.

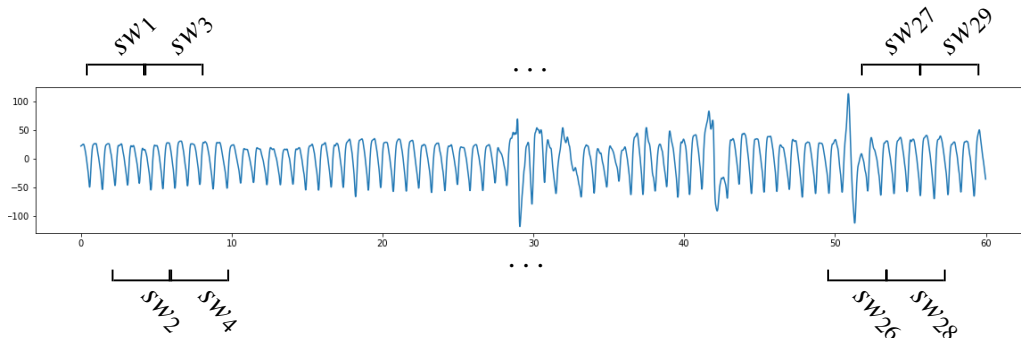


Figure 9: A sample 60-second BVP signal from the baseline condition of WESAD dataset.

## 5.2 Delay embeddings and persistent homology of subwindows

As we noted earlier in Section 3, different embedding dimensions detect different topological information about the time series (Figure 6). We used 4 levels of delay embedding dimensions (see Figure 10):  $.5fs$ ,  $fs$ ,  $1.5fs$ ,  $2fs$  where  $fs$  is the sampling frequency of the particular signal. For example, for a signal with  $fs = 100\text{Hz}$ , the set of embedding dimensions were  $\{50, 100, 150, 200\}$ .

After converting each subwindow to 4 different point clouds, the persistence diagrams of the induced Rips filtrations were computed for a maximum dimension of 1. Higher dimensional persistence diagrams were not computed since they require much more computational power, and we wanted to restrict our attention to connected components and one dimensional holes of the delay embeddings, but not to higher dimensional topological features.

In addition to the diagrams formed by the delay embeddings, two more persistence diagrams were computed: the 0 dimensional persistence diagrams created by the upper and lower level sets of the subwindows. Note that higher dimensional persistent homology cannot be computed from the subwindows, because the subwindows are univariate. Persistent homology of delay embeddings and level sets were computed using the Ripser [22] and Dionysus-2 libraries [14] of the Python programming language [24], respectively.

## 5.3 Feature engineering

Our methods have so far provided 6 persistence diagrams, 4 from delay embeddings and 2 for upper and lower level sets, for each subwindow. Then using the methods we outlined in Section 2.9, a total of 7 features were created from one homology class in a single persistence diagram. Since each subwindow yielded a total of 6 persistence diagrams and 4 diagrams coming from delay embeddings contained two homology classes, the total number of features created using persistent homology was 70.

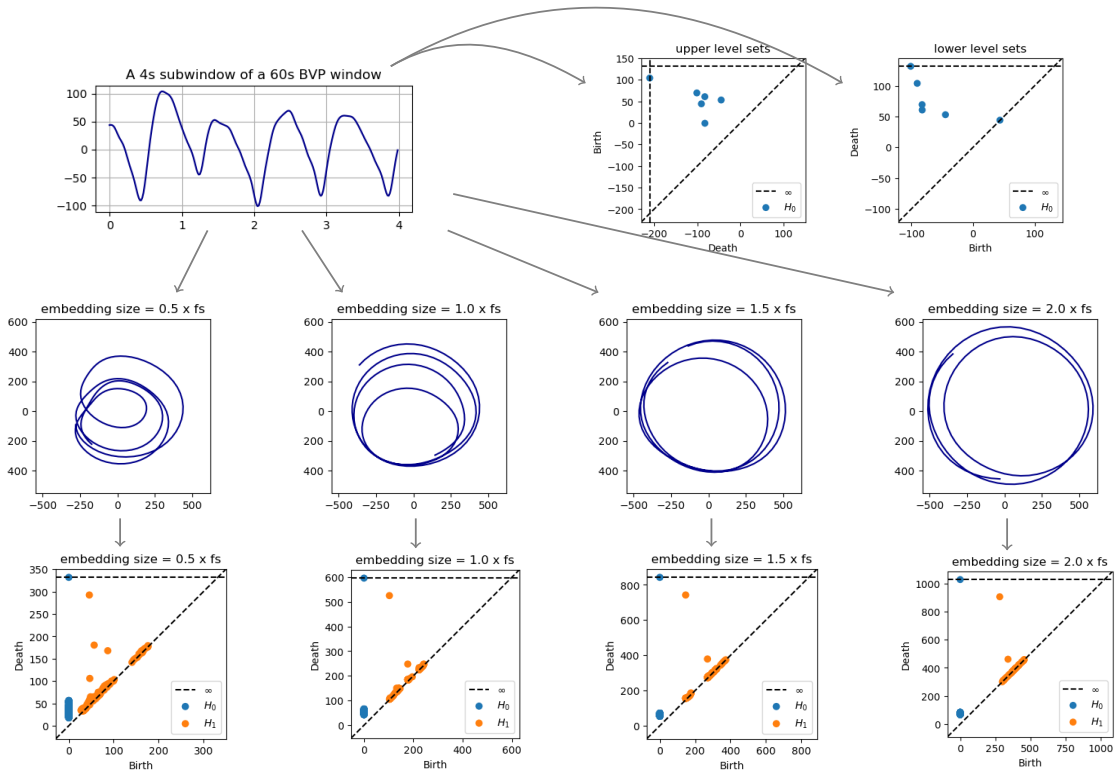


Figure 10: The pipeline for the computation of persistence diagrams from a subwindow.

In order to compute features for the 60s windows, the mean and standard deviation of the features obtained from (4s) subwindows were calculated. This allowed us to know how the signal behaves locally, and how this local behavior varies over a longer period. We also did the same for different window sizes (10, 20, 30, 60, 120, 180, 240 and 300 seconds), and specifically looked at how the recognition accuracies change accordingly.

The learning algorithms were tested on several subsets of features. For each of the four delay embedding sizes ( $.5fs$ ,  $1fs$ ,  $1.5fs$ ,  $2fs$ ) features from homology dimension zero ( $H_0$ ) and one ( $H_1$ ) were trained individually, and together. Similarly, features coming from upper and lower level sets were trained one by one and together. Then features from all delay embeddings and level sets were combined, and used as a full feature set. Before training the algorithms, constant features (*e.g.* full zeros) and features with a correlation higher than .9 were removed. Then, features were normalized to the range  $[0, 1]$  on both the training and the test set.

## 5.4 Learning algorithms

The original WESAD study used five classifiers, namely, a Decision tree, Random forest (RF), AdaBoost Decision Tree (AB), Linear discriminant analysis (LDA) and  $k$ -nearest neighbor. Three of them (RF, AB, LDA) attained highest accuracies for some signals. In addition to these three, we used a support vector classifier (SVC).

The tree based models (RF and AB) were trained on 100 trees with a maximum depth of 5, and the SVC model was trained with a linear kernel and a regularization parameter  $C = .1$ . We used

the scikit-learn library [16] implementations of the learning algorithms. For the reproducibility of our findings, we set the parameter `random_state = 0` in our stochastic models.

## 5.5 Cross-validation

For both datasets, we used binary (stress vs non-stress) and ternary classification models, and Leave One Subject Out Cross-Validation (LOSOCV) method. This method is similar to the k-fold cross validation if we let  $k$  to be the number of participants, and each fold to be a participant’s data. That is, the learning algorithm is trained on all subjects but one, tested on the remaining subject, and then the results are averaged. The biggest conceptual advantage of this method is that it helps us to know how the model performs on a previously unseen participant. Furthermore, no data leakage between the train and test test happens even when the sliding windows highly overlap.

In order to assess how much of the performance is due to individual differences, we also used an *intra-subject* cross-validation. For this, we consider only data from a single participant, split each condition in half, then use first halves to predict the second, and *vice versa*. The mean accuracy gives the accuracy for that subject, and averaging over all subjects gives the overall accuracy.

## 6 Results

We begin with the results of the classification problem with LOSOCV. Our findings showed that automatically created topological features distinguished different affect state conditions at least as good as the signal-specific features. Table 1 and Table 2 gives a summary of the results. Since the DriveDB dataset used 300-second non overlapping windows, in a Leave One Out Cross Validation (using intra- and inter- subject windows altogether), we cannot directly compare our findings with their original findings.

For the ternary classification problem (Table 1), the highest accuracies were obtained using a support vector classifier on topological features: 81.35% and 85.81% for WESAD and DriveDB datasets, respectively. The corresponding  $F_1$ -scores were 73.44% and 79.68%. For all signals in WESAD except chest and wrist TEMP, the automatically created features identified the affective states better than the original study. The most dramatic increase was found for the ACC signals: accuracies were improved more than 17% and 11% for the chest and wrist accuracies, respectively. This was followed by ECG, EMG and wrist EDA with corresponding accuracy enhancements 10%, 6% and 10%. Usually, the highest accuracies were attained when all topological features were combined as a full feature vector using an SVM classifier.

When we compare the confusion matrices of the ternary vs. binary class problems we see that our models performed better in distinguishing stress from non-stress. For the ternary class models, in WESAD the baseline and amusement conditions were well-separated from the stress condition while in DriveDB the city and highway conditions were well-separated from the relax condition.

For the binary case (Table 2), the highest accuracies reached were 94.46% and 98.07% for WESAD and DriveDB, respectively. The  $F_1$  scores corresponding to the highest accuracies

		.5×fs			1×fs			1.5×fs			2×fs			Level Sets			All	Original	
		Clf	H0	H1	Both	H0	H1	Both	H0	H1	Both	H0	H1	Both	Upper	Lower	Both	Dgms	Findings
<b>WESAD</b>																			
<i>Chest</i>																			
ACC	SVC	70.80	68.01	68.47	68.69	70.11	71.20	68.75	71.01	71.26	68.57	71.73	72.34	69.77	68.90	69.27	<b>74.47</b>	56.56	
ECG	SVC	71.08	65.95	70.68	75.24	74.19	<b>76.27</b>	70.73	65.30	69.64	64.32	67.30	69.50	66.11	65.29	65.85	72.72	66.29	
EMG	SVC	54.40	54.55	54.34	54.40	57.56	59.00	54.39	54.75	55.37	54.75	55.72	56.09	54.15	54.62	54.64	<b>59.67</b>	53.99	
EDA	LDA	56.41	66.31	61.81	58.58	61.06	63.27	57.23	57.44	56.61	58.96	61.04	60.06	66.45	66.25	66.26	<b>70.03</b>	67.07	
TEMP	LDA	54.51	54.75	53.45	54.33	54.75	53.09	54.69	50.73	49.06	54.45	51.25	49.78	53.02	48.38	48.67	48.92	<b>55.68</b>	
RESP	SVC	63.87	66.63	67.24	63.91	63.22	65.34	64.20	62.69	66.08	64.64	61.13	68.46	60.69	66.14	70.73	<b>75.57</b>	72.37	
<i>Wrist</i>																			
ACC	RF	67.31	66.81	68.02	67.43	65.03	66.80	67.07	63.95	65.59	67.45	65.45	66.33	67.28	67.08	67.17	<b>68.65</b>	57.20	
BVP	SVC	61.68	63.74	66.10	64.94	69.47	71.64	64.30	68.84	70.89	62.76	68.69	71.34	58.48	60.67	59.30	<b>73.41</b>	70.17	
EDA	RF	66.87	61.03	66.26	65.17	64.50	68.40	62.07	65.67	67.51	60.61	67.64	69.23	70.20	69.09	70.50	<b>72.02</b>	62.32	
TEMP	LDA	55.36	54.68	55.87	53.20	55.15	53.22	53.84	53.52	54.56	53.87	54.10	53.17	54.79	53.96	54.44	54.93	<b>58.96</b>	
All chest	SVC	74.42	68.27	70.11	<b>78.85</b>	72.84	75.02	76.32	63.14	73.09	75.09	70.28	74.11	75.28	75.34	74.98	77.96	76.50	
All wrist	RF	70.05	68.79	69.41	69.10	71.30	72.38	69.37	70.43	71.55	67.93	72.23	73.93	71.94	70.89	71.73	74.72	<b>75.21</b>	
All	SVC	75.61	69.75	72.94	78.89	78.42	80.63	75.81	70.11	78.66	76.10	75.23	76.13	79.61	80.56	79.99	<b>81.35</b>	79.57	
<b>DriveDB</b>																			
ECG	RF	49.95	51.71	52.16	49.76	52.51	51.49	51.97	52.65	52.38	42.23	53.32	52.91	<b>58.49</b>	57.02	57.46	56.68	-	
EMG	RF	65.49	63.16	66.87	65.72	60.91	64.15	65.53	60.35	62.90	63.37	63.00	63.61	<b>69.14</b>	67.74	68.36	66.49	-	
Foot GSR	RF	77.00	77.94	79.30	76.97	76.85	78.05	78.12	75.56	77.25	77.63	72.68	77.57	78.83	79.42	79.60	<b>80.08</b>	-	
Hand GSR	RF	64.74	65.53	65.97	66.76	61.03	66.20	66.37	55.08	66.48	<b>67.26</b>	57.14	66.30	65.42	65.03	65.42	65.80	-	
HR	SVC	50.54	56.77	56.24	49.60	59.30	59.02	46.75	56.86	57.75	46.83	58.56	58.69	58.39	57.71	59.80	<b>60.61</b>	-	
RESP	SVC	77.55	80.22	81.28	76.65	72.03	78.03	76.47	71.75	80.37	75.12	72.28	77.03	85.11	82.70	85.71	<b>85.81</b>	-	
All	SVC	76.68	82.50	80.80	76.01	73.05	76.01	74.80	76.74	77.05	74.24	73.89	76.63	83.84	84.64	<b>85.15</b>	80.59	-	

Table 1: Ternary classification problem accuracies.

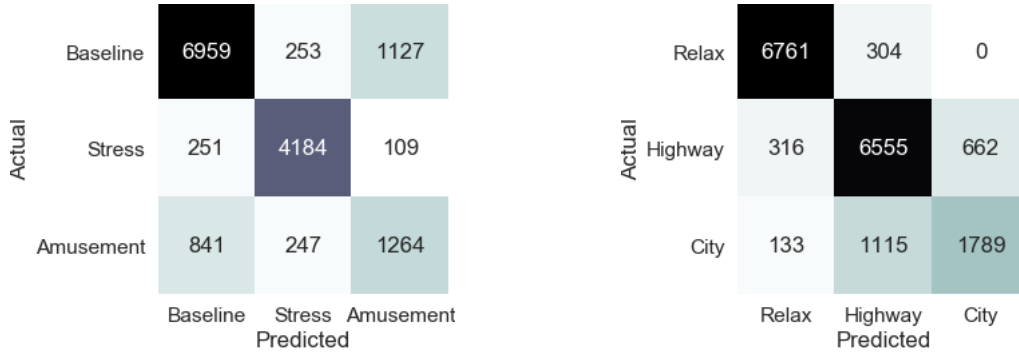


Figure 11: Confusion matrices for the three-class problem.

were 93.26% and 97.97%. For all signals but chest EDA and wrist BVP from WESAD, the topological features captured the differences better than the ones from the original study. Again, the ACC signals captured the stress state very well: the accuracy for chest increased by 14% and for wrist by 12%. ECG, EMG and wrist EDA improvements for the binary task were 3%, 6% and 5%.

In both ternary and binary classification tasks, we were able to attain very high accuracies with a small feature set. For instance, in WESAD dataset, the number of features coming from persistence diagrams of upper level sets of all modalities is 61 (a much smaller set of features than the one used in the original study), and we obtained 79.61% and 92.47% accuracies for the ternary and binary tasks with a support vector classifier.

Of course one would expect higher accuracies when the window size is larger. The sub-windowing method allowed us to run the same learning algorithms for different sliding window sizes without extra computational cost. For this purpose, we rerun the learning algorithms using several window lengths ranging from 10 to 300 seconds.

		.5xfs			1xfs			1.5xfs			2xfs			Level Sets			All	Original	
		Clf	H0	H1	Both	H0	H1	Both	H0	H1	Both	H0	H1	Both	Upper	Lower	Both	Dgms	Findings
<b>WESAD</b>																			
<i>Chest</i>																			
ACC	RF	<b>87.69</b>	85.47	84.93	83.66	78.51	80.88	84.70	80.38	79.75	87.10	80.64	81.98	84.54	83.34	84.82	84.18	73.87	
ECG	LDA	84.49	79.43	83.82	<b>88.70</b>	84.92	87.59	80.19	77.07	81.40	77.24	80.97	81.18	80.70	80.76	81.62	85.23	85.44	
EMG	LDA	71.35	71.69	72.05	70.96	72.15	<b>73.07</b>	70.24	70.41	71.70	69.68	71.54	72.80	66.99	68.03	67.14	69.75	67.10	
EDA	LDA	69.42	76.06	74.99	70.15	76.57	76.48	70.15	76.15	73.94	70.28	75.47	74.87	77.54	81.55	78.86	81.49	<b>81.70</b>	
TEMP	SVC	<b>70.19</b>	70.19	70.19	70.19	70.19	70.19	70.19	70.19	70.19	70.19	70.19	70.19	70.19	70.19	70.19	68.07	69.49	
RESP	LDA	77.92	80.61	81.72	78.37	78.32	79.62	78.72	75.39	77.93	78.26	71.46	77.98	80.48	81.73	87.75	<b>90.10</b>	88.09	
<i>Wrist</i>																			
ACC	RF	81.88	81.91	82.95	81.43	81.58	81.94	81.44	79.08	80.40	81.27	80.33	81.57	82.60	81.78	82.81	<b>83.52</b>	71.69	
BVP	LDA	77.30	79.87	80.06	80.41	82.37	85.21	79.86	78.12	83.92	78.99	75.85	83.04	71.67	72.51	71.93	84.03	<b>85.83</b>	
EDA	RF	79.70	74.83	78.38	77.63	78.55	80.98	76.80	78.95	79.49	76.02	79.65	81.19	84.01	82.78	83.70	<b>85.11</b>	79.71	
TEMP	RF	69.99	70.56	<b>71.44</b>	69.48	70.34	69.49	70.07	69.69	69.84	69.84	69.49	69.29	69.38	69.91	70.00	70.02	69.24	
All chest	SVC	88.03	85.96	86.67	89.32	88.09	86.28	88.78	82.56	83.84	86.00	86.01	87.33	90.91	91.97	91.09	91.79	<b>92.83</b>	
All wrist	SVC	86.18	83.11	85.67	85.00	85.33	86.85	82.83	87.36	88.29	81.62	87.48	<b>88.77</b>	86.07	87.04	86.48	88.55	87.12	
All	SVC	91.17	86.42	89.82	90.12	90.88	92.05	88.40	89.09	92.44	87.02	92.91	92.24	92.47	92.61	92.95	<b>94.46</b>	92.28	
<b>DriveDB</b>																			
ECG	RF	62.28	62.24	62.84	58.48	64.09	63.99	62.49	59.46	62.18	58.21	65.31	65.74	<b>71.11</b>	69.26	68.86	67.61	-	
EMG	RF	78.69	76.21	79.10	79.54	74.59	77.59	78.78	73.44	75.87	77.99	75.47	75.43	81.65	81.34	<b>82.04</b>	79.91	-	
Foot GSR	RF	89.46	90.67	90.83	88.88	90.73	90.28	89.55	89.68	88.93	89.61	83.92	89.21	<b>92.26</b>	91.59	91.64	91.88	-	
Hand GSR	RF	82.09	76.99	81.36	<b>82.47</b>	74.08	81.65	81.82	74.35	81.76	81.02	74.87	81.64	78.75	78.70	78.75	81.44	-	
HR	SVC	59.87	68.65	69.89	59.94	72.67	73.83	60.47	71.04	71.98	60.47	71.41	71.55	70.12	69.53	71.06	<b>74.67</b>	-	
RESP	RF	92.99	92.65	92.91	93.27	89.33	93.18	91.91	87.54	91.62	91.10	90.30	91.80	97.93	96.54	<b>98.07</b>	95.54	-	
All	RF	92.31	94.96	93.38	92.81	94.61	92.88	91.76	94.32	93.60	90.99	93.83	93.33	<b>96.24</b>	94.43	95.15	95.39	-	

Table 2: Binary classification problem accuracies.

Our intuition turned out to be true: longer window sizes implied higher accuracy for the most part. In particular, for the ternary classification problem (Figure 12), the accuracy for 300 second windows went up to 89.86% and 91.19% for WESAD and DriveDB, respectively. Similarly, for the binary classification problem (Figure 13), the accuracies for 300 second windows for WESAD and DriveDB were as high as 96.42% and 96.95%, respectively.

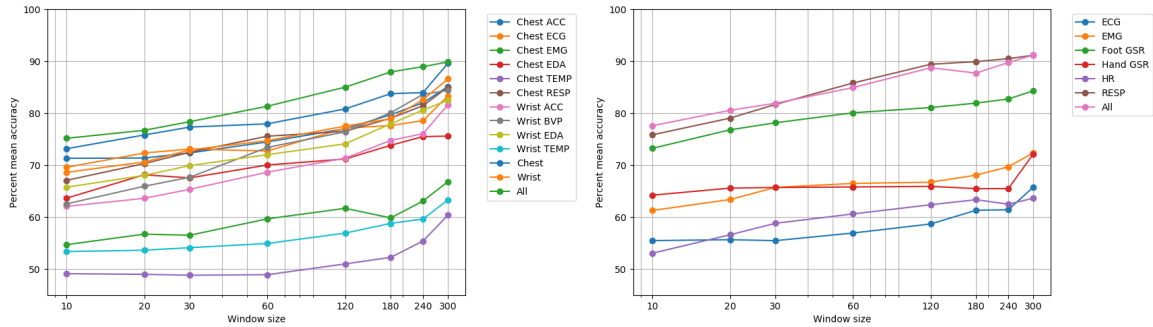


Figure 12: Ternary problem accuracies for different window sizes.



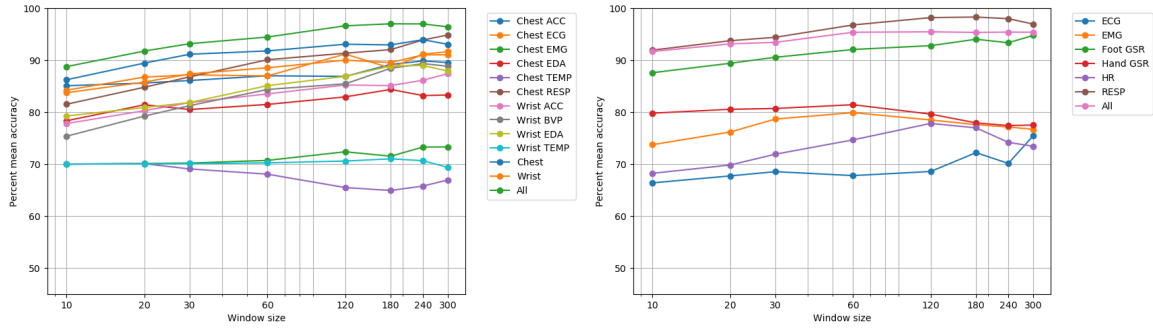


Figure 13: Binary problem accuracies for different window sizes.

All of the analyses above were done using LOSOCV. A curious question at this point is to ask how much of these errors stem from individual differences. To answer this question, we used an intra-subject cross-validation. We split each subject's data for each condition in two subsets where we used one half to develop a model while we used the other half to test, and *vice versa*. The sliding window size was again chosen to be 60 seconds. In Figure 14 and Figure 15 we compare these methods.

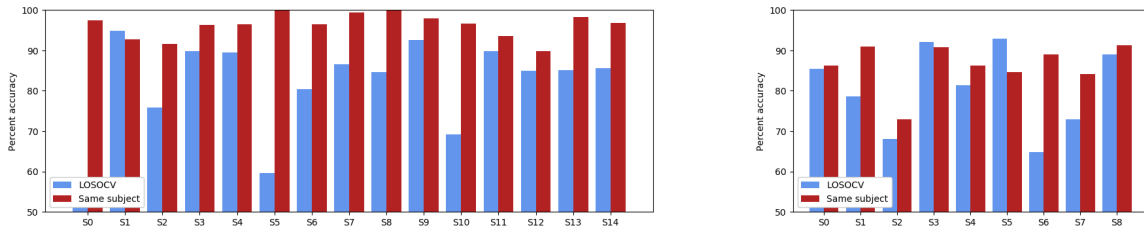


Figure 14: Ternary classification problem accuracies for LOSO and intra-subject cross validation.

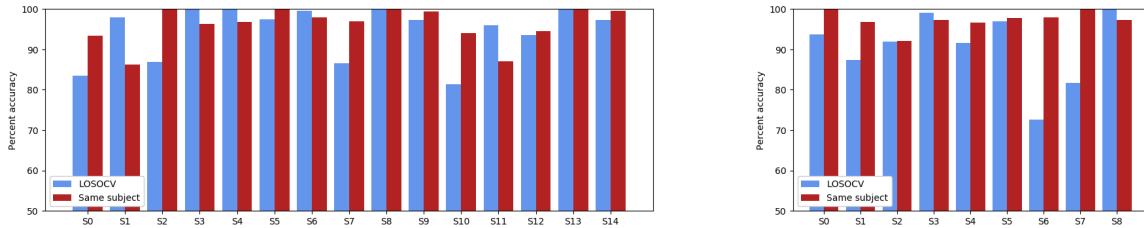


Figure 15: Binary problem accuracies for LOSO and intra-subject cross validation.

The difference was most pronounced in the three-class task. For instance, the mean accuracy increase for Subject 5 in WESAD was more than 40%. We ran four *t*-tests to test this effect. For the ternary problem in WESAD, accuracies obtained with intra-subjects CV (with mean 96.23%) was significantly higher than the ones for LOSOCV (with mean 81.35%) with significance  $p < .05$ . Although mean accuracies were higher for intra- rather than LOSO cross validation, the other *t*-tests did not reach statistical significance of  $p < .05$ . The null findings are probably due to the low number of subjects for the DriveDB, and the ceiling effect for the binary tasks. These findings indicate that when training and test sets contain data from the same subject, the learning algorithms perform better.

## 7 Conclusion

The main aim of this study was to demonstrate the power of Topological Data Analysis (TDA) techniques in classification of time series. Specifically, we used persistence diagrams and their statistical properties to distinguish physiological signals collected under stress and non-stress conditions. As common in previous studies, this was done by creating sliding windows of a fixed duration, computing features, and training and testing machine learning models on these engineered features. The subwindowing approach we developed allowed us to inspect how the signal behaves locally, and how this local behavior vary over longer periods. Then, using TDA methods we were able to create persistence diagrams from subwindows, create features on persistence diagrams and apply machine learning algorithms.

A proper feature engineering of a signal usually requires field knowledge. For instance, heart rate variability can be derived as a feature from an ECG signal. Our findings showed that most of the automatically generated topological features are at least as effective as signal specific features in affect recognition. The acceleration signals were found to be much more distinguished using the topological features compared to original WESAD findings. The mean accuracies were improved largely when either chest or wrist acceleration signals were used. Given that nearly all smartwatches and smartbands already have built-in accelerometer sensors, one can easily see that our method can readily, widely and cheaply be applied.

The features in this study came from four different delay embeddings and level sets which allowed us to make comparisons. The highest accuracies are obtained when we used features from all of the diagrams. Although this forces us to use a large number of features, it was possible to use features from only one delay embedding or level sets to get much fewer features, and obtain slightly less accuracy.

We have seen that longer windows usually implied higher recognition accuracy. However, this especially becomes computationally problematic when features are directly computed from the whole window. So, we implemented the subwindowing strategy which was previously used [12] on a different dataset with different feature engineering methods. Using this method, one computes features on the subwindows, then finds the window features by taking averages and standard deviations. We observed that once the mean and standard deviation of a window is known, and when an observation is replaced with a new one within the window, there is a relatively cheaper computing strategy for the new mean and standard deviation regardless of the window size. Using this observation, we can now use longer windows to compute new features from sliding windows and their subwindows to improve accuracy without incurring heavy computational costs.

Our findings also indicate that when the learning algorithm is trained and tested on disjoint data subsets coming from the same subject, the accuracies are higher than the LOSOCV approach. Hence, a device monitoring stress from a person may start with a relatively lower recognition accuracy, but is going to improve its discriminative power when worn by the same person for long enough to update the parameters of the learning algorithm. In the original DriveDB study, the authors used 300 second non-overlapping windows with leave one out cross validation (using both intra- and inter-subjects data) and reached approximately 97% accuracy. When we trained our model on 300 second windows with LOSOCV, we reached higher than 91% accuracy with fewer features. Given that we only included 9 subjects (compared to 24 in the original study) due to missing data and we used LOSOCV, our finding are promising.

## 7.1 Future work

This work used a single subwindow size for every stress condition in the signal. For future works, one can manipulate the subwindow size of a periodic signal and make sure that the delay embedding contains one and only one closed loop. Furthermore, in addition to the  $\varepsilon$  parameter in the Rips filtration, one can compute the multiparameter persistent homology where the dataset grows with time in the other dimension. Lastly, one can use other vector representations of persistence diagram, and/or combine them with classical signal-specific features to obtain even higher accuracies.

## References

- [1] Fatih Altındaş, Bülent Yılmaz, Sergey Borisenok, and Kutay İçöz. Parameter investigation of topological data analysis for eeg signals. *Biomedical Signal Processing and Control*, 63:102196.
- [2] Nieves Atienza, Luis M Escudero, Maria Jose Jimenez, and M Soriano-Trigueros. Persistent entropy: a scale-invariant topological statistic for analyzing cell arrangements. *arXiv preprint arXiv:1902.06467*, 2019.
- [3] A. Björner. Topological methods. In *Handbook of combinatorics, Vol. 1, 2*, pages 1819–1872. Elsevier Sci. B. V., Amsterdam, 1995.
- [4] Peter Bubenik. Statistical topological data analysis using persistence landscapes. *The Journal of Machine Learning Research*, 16(1):77–102, 2015.
- [5] Frédéric Chazal, Vin De Silva, Marc Glisse, and Steve Oudot. The structure and stability of persistence modules. *arXiv preprint arXiv:1207.3674*, 21, 2012.
- [6] David Cohen-Steiner, Herbert Edelsbrunner, and John Harer. Stability of persistence diagrams. *Discrete & Computational Geometry*, 37(1):103–120, 2007.
- [7] David Cohen-Steiner, Herbert Edelsbrunner, John Harer, and Yuriy Mileyko. Lipschitz functions have 1 p-stable persistence. *Foundations of computational mathematics*, 10(2):127–139, 2010.
- [8] Alireza Dirafzoon, Namita Lokare, and Edgar Lobaton. Action classification from motion capture data using topological data analysis. In *2016 IEEE global conference on signal and information processing (globalSIP)*, pages 1260–1264. IEEE, 2016.
- [9] Herbert Edelsbrunner, David Letscher, and Afra Zomorodian. Topological persistence and simplification. In *Proceedings 41st annual symposium on foundations of computer science*, pages 454–463. IEEE, 2000.
- [10] Saba Emrani, Thanos Gentimis, and Hamid Krim. Persistent homology of delay embeddings and its application to wheeze detection. *IEEE Signal Processing Letters*, 21(4):459–463, 2014.

- [11] Jennifer A Healey and Rosalind W Picard. Detecting stress during real-world driving tasks using physiological sensors. *IEEE Transactions on intelligent transportation systems*, 6(2):156–166, 2005.
- [12] Florian Höning, Anton Batliner, and Elmar Nöth. Fast recursive data-driven multi-resolution feature extraction for physiological signal classification. In *3rd Russian-Bavarian Conference on Bio-medical Engineering*, pages 47–52, 2007.
- [13] Andrew Marchese and Vasileios Maroulas. Signal classification with a point process distance on the space of persistence diagrams. *Advances in Data Analysis and Classification*, 12(3):657–682, 2018.
- [14] Dmitriy Mozorov. Dionysus 2. URL: <https://mrzv.org/software/dionysus2/>.
- [15] Nina Otter, Mason A. Porter, Ulrike Tillmann, Peter Grindrod, and Heather A. Harrington. A roadmap for the computation of persistent homology. *EPJ Data Science*, 6(17), 2017.
- [16] Fabian Pedregosa, Gaël Varoquaux, Alexandre Gramfort, Vincent Michel, Bertrand Thirion, Olivier Grisel, Mathieu Blondel, Peter Prettenhofer, Ron Weiss, Vincent Dubourg, et al. Scikit-learn: Machine learning in python. *the Journal of machine Learning research*, 12:2825–2830, 2011.
- [17] Jose A Perea and John Harer. Sliding windows and persistence: An application of topological methods to signal analysis. *Foundations of Computational Mathematics*, 15(3):799–838, 2015.
- [18] Chi Seng Pun, Kelin Xia, and Si Xian Lee. Persistent-homology-based machine learning and its applications—a survey. *arXiv preprint arXiv:1811.00252*, 2018.
- [19] Philip Schmidt, Attila Reiss, Robert Duerichen, Claus Marberger, and Kristof Van Laerhoven. Introducing wesad, a multimodal dataset for wearable stress and affect detection. In *Proceedings of the 20th ACM International Conference on Multimodal Interaction*, pages 400–408, 2018.
- [20] Lee M Seversky, Shelby Davis, and Matthew Berger. On time-series topological data analysis: New data and opportunities. In *Proceedings of the IEEE conference on computer vision and pattern recognition workshops*, pages 59–67, 2016.
- [21] Floris Takens. Detecting strange attractors in turbulence. In *Dynamical systems and turbulence, Warwick 1980*, pages 366–381. Springer, 1981.
- [22] Christopher Tralie, Nathaniel Saul, and Rann Bar-On. Ripser. py: A lean persistent homology library for python. *Journal of Open Source Software*, 3(29):925, 2018.
- [23] Yuhei Umeda. Time series classification via topological data analysis. *Information and Media Technologies*, 12:228–239, 2017.
- [24] Guido Van Rossum and Fred L Drake Jr. *Python reference manual*. Centrum voor Wiskunde en Informatica Amsterdam, 1995.